PHYSICAL REVIEW B **99**, 094409 (2019)

Editors' Suggestion

Domain-wall motion and interfacial Dzyaloshinskii-Moriya interactions in Pt/Co/Ir(t_{Ir})/Ta multilayers

Kowsar Shahbazi,[1,*] Joo-Von Kim,[2] Hans T. Nembach,[3] Justin M. Shaw,[3] Andreas Bischof,[4] Marta D. Rossell,[4,5]
Vincent Jeudy,[6] Thomas A. Moore,[1] and Christopher H. Marrows[1,†]
[1]*School of Physics and Astronomy, University of Leeds, Leeds LS2 9JT, United Kingdom*
[2]*Centre for Nanoscience and Nanotechnology (C2N), CNRS, Université Paris-Sud, Université Paris-Saclay, 91120 Palaiseau, France*
[3]*Quantum Electromagnetics Division, National Institute of Standards and Technology, Boulder, Colorado 80305, USA*
[4]*IBM Research-Zurich, Säumerstrasse 4, CH-8803 Rüschlikon, Switzerland*
[5]*Electron Microscopy Center, Empa, Swiss Federal Laboratories for Materials Science and Technology, Überlandstrasse 129, 8600 Dübendorf, Switzerland*
[6]*Laboratoire de Physique des Solides, CNRS, Université Paris-Sud, Université Paris-Saclay, 91405 Orsay Cedex, France*

(Received 9 October 2018; revised manuscript received 21 December 2018; published 7 March 2019)

The interfacial Dzyaloshinskii-Moriya interaction (DMI) is important for chiral domain walls (DWs) and for stabilizing magnetic skyrmions. We study the effects of introducing increasing thicknesses of Ir, from zero to 2 nm, into a Pt/Co/Ta multilayer between the Co and Ta layers. There is a marked increase in magnetic moment, due to the suppression of the dead layer at the interface with Ta, but the perpendicular anisotropy is hardly affected. All samples show a universal scaling of the field-driven DW velocity across the creep and depinning regimes. Asymmetric bubble expansion shows that DWs in all of the samples have the left-handed Néel form. The value of in-plane magnetic field at which the creep velocity shows a minimum drops markedly on the introduction of Ir, as does the frequency shift of the Stokes and anti-Stokes peaks in Brillouin light scattering (BLS) measurements. Despite this qualitative similarity, there are quantitative differences in the DMI strength given by the two measurements, with BLS often returning higher values. Many features in bubble expansion velocity curves do not fit simple models commonly used, namely a lack of symmetry about the velocity minimum and no difference in velocities at high in-plane fields. These features are explained by the use of a new model in which the depinning field is allowed to vary with in-plane field in a way determined from micromagnetic simulations. This theory shows that the velocity minimum underestimates the DMI field, consistent with BLS giving higher values. Our results suggest that the DMI at an Ir/Co interface has the same sign as the DMI at a Pt/Co interface.

DOI: 10.1103/PhysRevB.99.094409

I. INTRODUCTION

Whilst hard disks still dominate the data storage landscape in terms of volume of data stored, they feature moving parts that increase energy consumption and decrease reliability. Magnetic domain walls (DWs) and skyrmions are the smallest magnetic components that can be used in a new generation of magnetic recording media/processing devices (so-called racetrack memories) to overcome these obstacles [1,2]. To be able to make use of them efficiently, one of the most important parameters to optimize and control is the interfacial Dzyaloshinskii-Moriya interaction (DMI). The DMI changes the magnetostatically favorable Bloch walls to Néel walls with a fixed chirality [3] in multilayers with perpendicular magnetic anisotropy (PMA) which in turn makes them sensitive to spin-orbit torques [4] so that they can be moved by current pulses.

The first step towards optimization of any parameter is to be able to measure it easily and reliably. Several different methods have been used to evaluate the strength of the DMI, *D*. Current-driven domain wall motion under in-plane (IP) applied field has been widely investigated [5–8]. But using current to study DMI complicates the situation because usually the spin Hall effect, Rashba effect, and DMI are present simultaneously [9]. Microscopy measurements such as spin-polarized scanning tunneling microscopy [10], spin-polarized low-energy electron microscopy [11], and photoemission electron microscopy combined with x-ray magnetic circular dichroism [12] can also be used, but they are suitable only for particular kinds of samples. Brillouin light scattering (BLS) uses nonreciprocal propagation of spin waves in materials with DMI to measure *D* [13,14], but the limited availability of BLS apparatus means that is not suitable for routine measurements of large numbers of samples.

One widely adopted technique to estimate DMI is asymmetric bubble expansion since it requires minimal sample preparation and relatively inexpensive equipment to implement. The concept was introduced by Je *et al.* [15] and extended by Hrabec *et al.* [16]. It was known that the DMI in systems with broken inversion symmetry splits the degeneracy between right-handed and left-handed twists in the magnetization and enforces homochiral Néel walls in layers

---

[*] pyks@leeds.ac.uk

[†] c.h.marrows@leeds.ac.uk

with perpendicular magnetic anisotropy if it is sufficiently strong. As a result, the DMI can be represented as an intrinsic field across the DW [3]. The central idea of the asymmetric bubble expansion method is that this intrinsic field may be enhanced or partially/completely canceled by an externally applied in-plane field. This affects the wall energy and hence its creep velocity under an out-of-plane (OP) field. Elongation of domains in an IP field was imaged decades ago in garnet bubble domain materials [17] and was described in detail by de Leeuw, van den Doel, and Enz [18]. Still, the very first time DMI was suggested as one of the probable causes of this elongation was by Kabanov *et al.* in 2010 [19]. They noticed changes of DW velocity with IP applied field and variation of elongation direction with field sign. Likewise, Je *et al.* [15] attributed the asymmetrical growth of bubble domains to breaking of DMI related Néel wall radial symmetry on either side of an expanding bubble with IP field. Typically curves for the DW creep velocity v as a function of in-plane applied field H_{IP} are measured and fitted to a simple creep model to reveal the DMI field H_{DMI} and hence D. Whilst experimentally straightforward, interpretation of the results has not always been easy. Some literature reported excellent matches for this model [20–23], but other experimental investigations revealed that basic assumptions of the model are not necessarily correct for all PMA materials. For instance, Soucaille *et al.* mentioned a change in their domain wall roughness with IP field [24]. Nevertheless, a common difficulty is simply that the $v(H_{\mathrm{IP}})$ curves sometimes do not have the simple form expected [24–29]. To overcome this problem, some researchers went to the extent of applying fast pulses of high fields to work in the flow regime [26] or doing complex analytical calculations of the DW energy for the whole bubble [30]. All in all, using a simple creep model to evaluate DMI from asymmetrical bubble expansion is not always as straightforward as first thought, and there are anomalies that require further study.

Here we investigate asymmetric bubble expansion to evaluate DMI in a heavy metal (HM)/ferromagnet (FM) multilayer by systematic change of one parameter in a sample series, highlighting some anomalies that cannot be described by the simple creep model. Moreover, since DW dynamics will affect the behavior of the bubble propagation, we also performed an extensive investigation of the details of DW dynamics in the creep and depinning regimes. By combining these results in a model in which the wall creep velocity depends on the depinning field that separates these regimes, which in turn depends on H_{IP}, we are able to demonstrate the origin of two of these anomalies, namely the lack of symmetry of $v(H_{\mathrm{IP}})$ curves about their minima, and the tendency for these curves to join together at high fields. This model also shows that the field at which the minimum in $v(H_{\mathrm{IP}})$ occurs underestimates H_{DMI}. We also compare our results for D from asymmetric bubble expansion with those from BLS measurements on the same set of samples.

The multilayers we chose to study had the form Pt/Co/Ir(t_{Ir})/Ta, in which the only quantity varied was the thickness t_{Ir} of the Ir layer. The presence of Ir brings another aspect to this work: Pt/Co/Ta multilayers show a high net spin Hall angle [31] and DMI-stabilized skyrmion structures have been reported in them [32]. Both the net spin Hall angle and the net DMI D arise from differences between the effects arising of the heavy metal layers above and below the Co. Where Pt and Ta have large and opposite spin Hall angles, giving a large overall difference [31], the same may not be true of the DMI. The Pt/Co interface has been already shown to exhibit a sizable DMI [14,33]. On the other hand, a Co/Ta interface is expected to have a low DMI with the same sign as the Co/Pt interface [33,34], so the resulting DMI of such multilayers is less than what one can get with a single Pt/Co interface. On the other hand, the DMI at an Ir/Co interface is predicted to be large and have the opposite sign to that for a Pt/Co interface [34], motivating Pt/Co/Ir as the basis for skyrmion-bearing multilayers [35,36]. Considering the fact that the spin Hall effect takes place throughout the bulk of a heavy metal layer, whereas the DMI is generated at an interface, inserting Ir at the interface where retaining Ta for the bulk of the layer appears attractive to combine the two effects. Nevertheless, doubts have been raised about the actual sign of the DMI for an Ir/FM interface [28,37]. Here we go into the detail of the effect of inserting Ir and compare our results with other reports.

II. EXPERIMENT

A. Sample growth and measurement methods

Multilayers with a nominal structure of Ta(2.0)/Pt(2.2)/Co(0.8)/Ir(t_{Ir})/Ta(4.0) (layer thicknesses in nm) were deposited onto thermally oxidized silicon substrates by dc magnetron sputtering [Fig. 1(a)] in a single vacuum cycle of the sputtering chamber. The Ir thickness t_{Ir} varied from 0 to 2.0 nm with all other parameters being held constant. The base pressure was below 2×10^{-5} Pa and the deposition Ar pressure was 0.4 Pa. The substrates were at room temperature and samples did not experience any annealing treatment.

High-resolution scanning transmission electron microscopy (STEM) and energy-dispersive x-ray (EDX) spectroscopy measurements were carried out to investigate the quality of the deposition and interface sharpness in the material stack. The measurements were performed at 300 kV employing a spherical-aberration-corrected STEM instrument equipped with four windowless silicon drift detectors for high-sensitivity EDX analysis. A probe semiconvergence angle of 24.6 mrad and an annular semidetection range of the annular dark-field detector set to collect electrons scattered between 53 and 200 mrad were used. The cross-section lamellae for the STEM-EDX investigations were prepared with a focused ion-beam (FIB) instrument operating at accelerating voltages of 30 and 5 kV and were about 50 nm thick. To minimize possible damage to the stack structure, the sample was protected with a 200-nm-thick sputtered Pt layer before inserting it into the FIB. The high-angle annular dark-field (HAADF) STEM image in Fig. 1(b) shows easily distinguishable layers from the different materials, with the corresponding EDX elemental line profiles aligned with each layer. Partial oxidation of the Ta top layer due to the exposure to air can also be seen, proving that the capping layer was thick enough to prevent oxidation of the inner layers.

Perpendicular hysteresis loops of the samples were measured with the polar magneto-optical Kerr effect (P-MOKE). The field sweep rate was 2 mT/s, slow enough for the loops

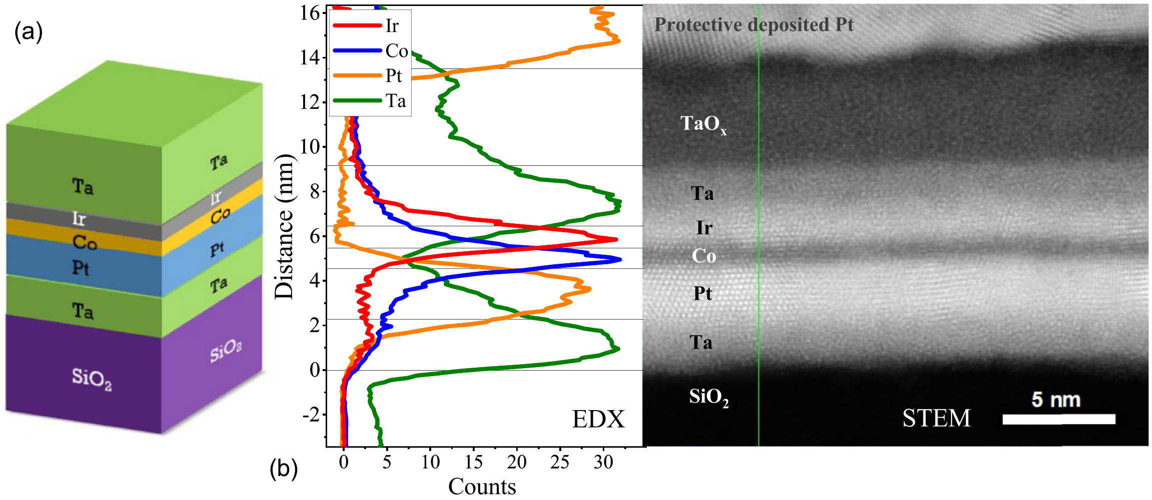

FIG. 1. Magnetic multilayer structure. (a) Schematic of the multilayer stack, nominally Ta(2.0)/Pt(2.2)/Co(0.8)/Ir(t_{Ir})/Ta(4.0) (layer thicknesses in nm). (b) EDX elemental line profiles across the multilayer structure with 1.0 nm Ir alongside a HAADF image of the same sample. The different interfaces and a smooth growth of the layers are clearly visible.

to be considered quasistatic. The anisotropy field, H_K, and saturation magnetization, M_s, were determined from hysteresis loops with an IP field measured using superconducting quantum interference device-vibrating sample magnetometry (SQUID-VSM).

Symmetric bubble expansion, the growth of bubble domains in the presence only of an OP driving field, was imaged at room temperature using a wide-field Kerr microscope to study DW dynamics in the crossover from the creep to the viscous flow regime. To apply the OP field, a small coil (∼100 turns and ∼1 mm diameter) was carefully placed on top of the film surface. DW propagation using high driving fields could not be reached because of multiple domain nucleations and merging domains during pulse time. Using P-MOKE microscopy, one can measure the distance domain walls propagate during an OP field pulse of known duration, and hence the velocity of the domain walls can be estimated. The results that we show are an average of 3–5 repeats for each applied field.

Asymmetric bubble expansion was studied at room temperature by the same method as above, but with the addition of an extra electromagnet capable of supplying an IP field of up to $\mu_0 H_x = 250$ mT and a homemade OP field coil that can apply field of up to $\mu_0 H_{\mathrm{OP}} = 40$ mT. For this part, the symmetry-breaking IP field is kept constant and OP driving field is pulsed to expand the bubble step by step. The DW velocity here is measured for the walls perpendicular to IP field, as discussed in previous investigations [21,29]. [Example Kerr difference images are discussed later and shown in Fig. 6(d).] In this arrangement, the applied IP field enhances or cancels the DMI field, allowing the DMI strength D to be measured.

The asymmetric frequency shift arising from the annihilation or generation of spin waves (SWs) in a ferromagnet with DMI was also used to measure D using Brillouin light scattering (BLS) in the Damon-Eshbach geometry at room temperature with a fixed wave vector of $k = 16.7\ \mu\mathrm{m}^{-1}$. The laser has a spot size of 39 μm (full width at half maximum of a Gaussian beam profile) when in perpendicular incidence. The measurement was done with a 45° incidence angle. This frequency shift asymmetry was determined by measuring for both field polarities.

B. Magnetic characterization

All the Pt/Co(0.8)/Ir(t_{Ir})/Ta multilayers showed square P-MOKE hysteresis loops for every value of t_{Ir}, as presented in Fig. 2(a). The OP coercive field initially increases with t_{Ir}, has a peak value for $t_{\mathrm{Ir}} = 0.4$ nm, but then decreases and reaches

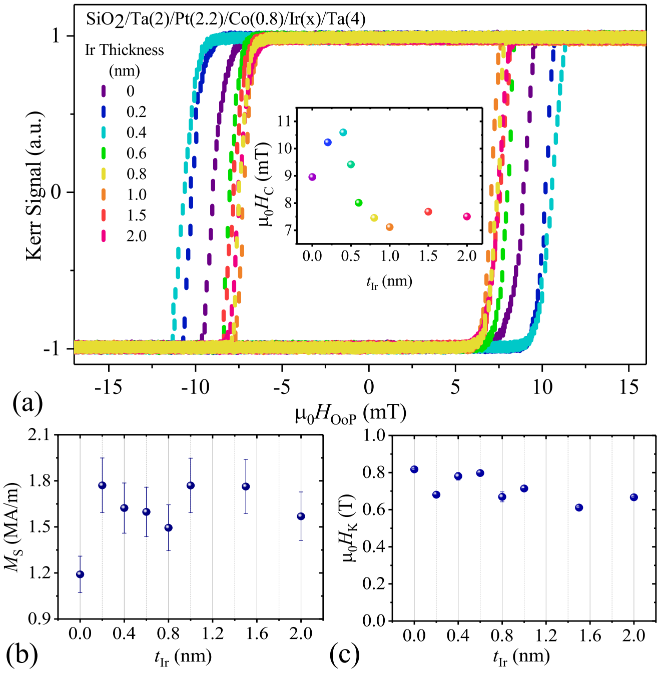

FIG. 2. Magnetic characterization. (a) Polar Kerr measurements show clear square-shaped hysteresis loops confirming strong PMA. The probed area is the size of our unfocussed laser spot, which is of millimeter scale. (b) Saturation magnetization M_S and (c) anisotropy field H_K as a function of Ir thickness t_{Ir}; both are determined from hysteresis loops acquired by SQUID-VSM with an in-plane field.

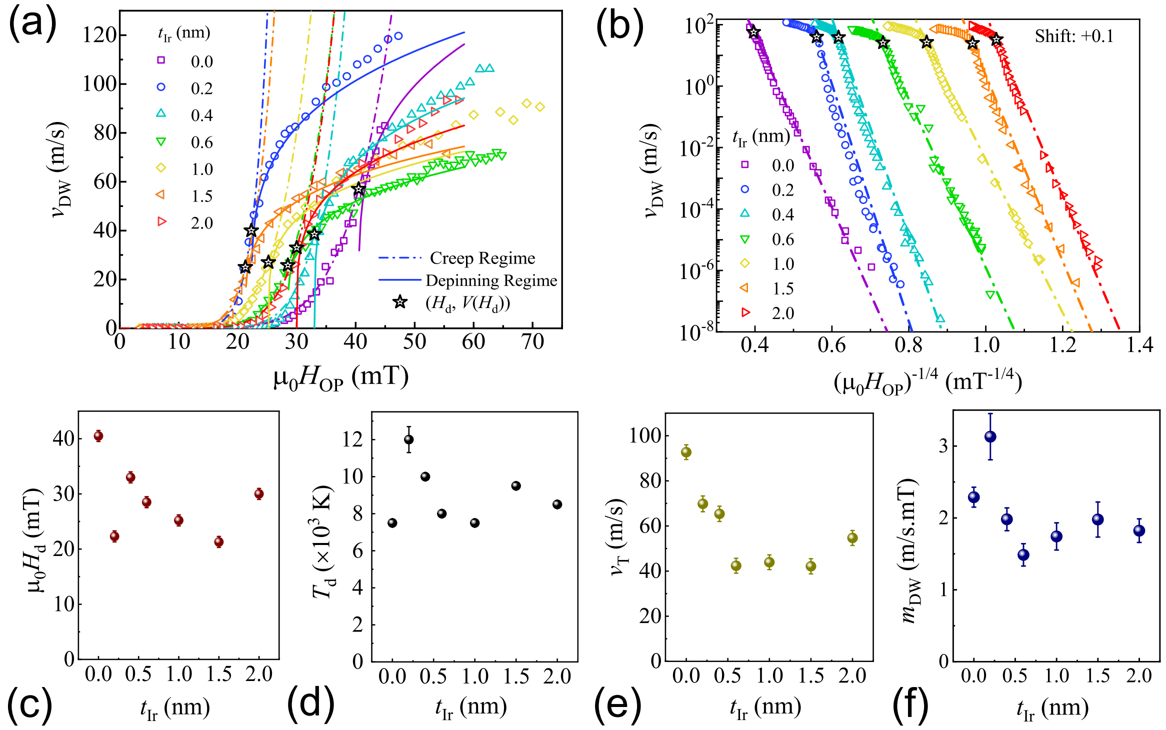

FIG. 3. Field-induced domain wall motion. (a) DW velocity v as a function of OP applied field $\mu_0 H_{\mathrm{OP}}$ for multilayers with increasing t_{Ir} along with the fits to creep and depinning universal functions (dashed-dot and solid lines, respectively). The stars show the inflection point which corresponds to the depinning field, H_d. (b) log v as a function of scaled driving field to highlight the compatibility of experimental data to the universal creep law. Each set of data is horizontally shifted for a clearer presentation. The (c) depinning field H_d, (d) depinning temperature T_d, (e) disorder-free depinning velocity v_T, and (f) DW magnetic mobility m_{DW}, each as a function of Ir thickness.

a constant level for $t_{\mathrm{Ir}} > 0.6$ nm, likely to be around the point where the Ir becomes thick enough to form a continuous layer.

Figures 2(b) and 2(c) also show the changes of saturation magnetization, M_s, and anisotropy field, H_K, with Ir thickness. M_s jumps up as soon as there is any Ir in the stack and stays almost constant for higher t_{Ir}. This suggests the presence of a dead layer between Co and top Ta layer, which is believed to be a result of intermixing between Ta and the ferromagnetic layer [38–41], as well as a small degree of proximity magnetism in the Ir [42]. The dead layer causes a reduction of effective thickness of the magnetic material. The M_s of the samples with Ir has the average value of $M_{s,\mathrm{avg}} = 1.7 \pm 0.1$ MA/m, calculated on the basis that only the volume of the Co layer is taken into account. H_K decreases slightly with t_{Ir}, but has a weak dependence on t_{Ir}.

A temperature dependent measurement of saturation magnetization was also fitted by the Bloch law to estimate the exchange stiffness constant, A. The measurements for multilayers with $t_{\mathrm{Ir}} = 0.0$ and 0.4 nm resulted in an average value of $A = 17 \pm 2$ pJ/m for the two samples, which is in good agreement with our previous measurements [29]. Example data are shown in Appendix A.

C. Domain wall velocity

Field-induced domain wall motion (FIDWM) was studied for all of the films. Figure 3 shows the changes of DW velocity v with increasing applied OP field for stacks with different t_{Ir}. DW dynamics are classified into different regimes of motion including the creep, depinning, and flow regimes [43]. In very low fields, the applied field is not enough to overcome the pinning barrier and move the DW. So, when $T \neq 0$, thermal excitations can assist the field and cause a very slow motion of DWs known as creep. For fields higher than the so-called depinning field, H_d, DW dynamics changes to a form known as the depinning regime. In both the creep and depinning regimes, thermal activation and the pinning potential dictate the DW movement. For a high enough drive field, the DW moves into a viscous flow regime that is independent of pinning force and temperature, and is only limited by dissipation.

As Fig. 3(b) shows, for fields lower than H_d, v rises by nine orders of magnitude within a 10 mT field span, which is characteristic of creep regime behavior. The linear change of $\ln v$ vs $H_{\mathrm{OP}}^{-1/4}$ confirms the creep motion of the DWs in this field range [44], confirming the validity of assuming DW as a one-dimensional elastic interface progressing in a two-dimensional medium with random-bond short-range pinning potential [45,46]. (In Appendix B we show that this remains true even under the simultaneous application of an in-plane field.) For fields higher than H_d, the measured velocities are in the depinning regime. All the data were fitted simultaneously with universal functions of creep and depinning motion of DW to evaluate the three material-dependent pinning parameters: depinning temperature, T_d, depinning field, H_d, and disorder-free velocity at the depinning field, v_T [46,47]. These fits are shown in Fig. 3(a), and the parameters extracted from them are plotted in Figs. 3(c), 3(d) and 3(e). It appears that for larger Ir thicknesses, i.e., $t_{\mathrm{Ir}} > 0.5$ nm, each of these values

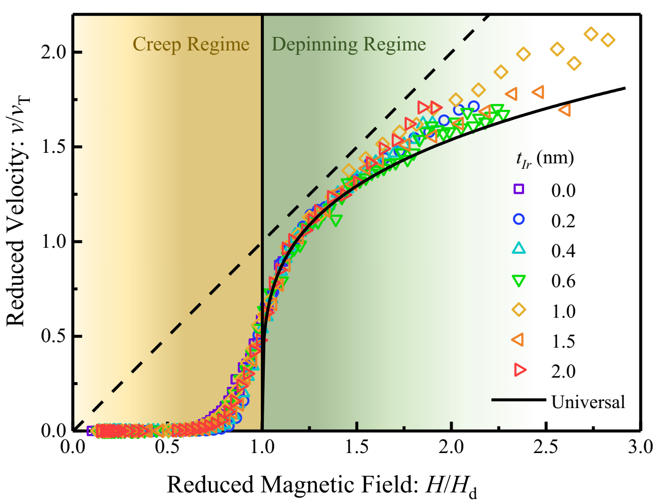

FIG. 4. Reduced velocity vs reduced field for different Ir thicknesses t_{Ir}, showing a good universal collapse of the curves. The tilted dashed line represents the linear flow regime in which $v/v_T = H_{\mathrm{OP}}/H_{\mathrm{d}}$. The vertical solid line separates the creep and depinning regime. The solid curve marks the universal depinning transition which is conforming to all experimental data in the $1 < H_{\mathrm{OP}}/H_{\mathrm{d}} < 1.5$ range. All the samples leave the universal depinning regime at some point after $H_{\mathrm{OP}}/H_{\mathrm{d}} \approx 1.5$ and begin to approach the flow regime.

stays roughly constant, while for $t_{\mathrm{Ir}} < 0.5$ nm the parameters do not follow a monotonic change. This suggests that the Ir layer does not affect the DW dynamics significantly after it exceeds 0.5 nm in thickness. The estimated T_{d} and H_{d} are ~3 and 4 times lower than the reported values for Au/Co/Au [48] at room temperature, respectively, which indicates less average pinning in the films.

By plotting the reduced velocity, $v_{\mathrm{DW}}/v_{\mathrm{T}}$, as a function of reduced driving field, $H_{\mathrm{OP}}/H_{\mathrm{d}}$, shown in Fig. 4, one can see that all the data collapse onto one curve, emphasizing the good agreement with universal depinning behavior. This agreement holds over a large range of $1 < H_{\mathrm{OP}}/H_{\mathrm{d}} < 1.5$ that is comparable to the previous universality range (up to 1.3 at room temperature) reported for Pt/Co/Pt trilayers [48].

We were not able to fully enter the flow regime for any of the multilayers, due to multiple nucleation sites and the merging of bubble domains in high fields for the shortest available pulses. Nevertheless, we can estimate the DW dynamics in the flow regime using the material dependent parameters extracted from our fits. The depinning velocity, v_{T}, is defined as the velocity of DW with H_{d} as driving force in the absence of pinning in the film. Knowing that, the mobility of the DW can be calculated as $m_{\mathrm{DW}} = \mu_0^{-1} v_{\mathrm{T}}/H_{\mathrm{d}}$, according to Ref. [47]. This is plotted in Fig. 3(f) for each of our samples. With the exception of the sample with $t_{\mathrm{Ir}} = 0.2$ nm, this parameter is roughly constant, with an average of $m_{\mathrm{DW,avg}} = (1.8 \pm 0.2) \times 10^3\ \mathrm{ms^{-1}T^{-1}}$, which is close to the DW mobility for Au/Co(0.8)/Au in Ref. [49]. Using the DW mobility, the Gilbert damping parameter can also be determined from $m_{\mathrm{DW}} = \gamma\Delta/\alpha$ for steady flow, or $m_{\mathrm{DW}} = \gamma\Delta/(\alpha + \alpha^{-1})$ for precessional flow, where $\Delta = \sqrt{A/K_{\mathrm{eff}}}$ is the DW thickness and γ is the gyromagnetic ratio. As there was no solution for the precessional regime, the linear flow regime is proved to correspond to steady flow for all the samples, with the average damping value of $\alpha = 0.48 \pm 0.01$, which, although high, is of a comparable order of magnitude to other results for Pt/Co multilayers [43].

D. Dzyaloshinskii-Moriya interaction

Multilayers of Co with PMA often have bubble domains. In the presence of DMI there will be an effective in-plane field H_{DMI} acting on the DW surrounding the bubble. The interaction of an applied in-plane field H_{IP} with H_{DMI} will affect the growth rate of opposite parts of the bubble domain, and so can be used for evaluation of the DMI strength and sign [15,16]. According to Je *et al.* [15], the energy density σ_{DW} of the DW can be written as

$$\sigma_{\mathrm{DW}}(H_{\mathrm{IP}}) = \sigma_0 - \frac{\pi^2 \Delta M_{\mathrm{S}}{}^2}{8K_{\mathrm{D}}}(H_{\mathrm{IP}} + H_{\mathrm{DMI}})^2, \tag{1}$$

when $|H_{\mathrm{IP}} + H_{\mathrm{DMI}}| < (4K_{\mathrm{D}}/\pi M_{\mathrm{S}})$, i.e., where the sum of IP and DMI fields is not big enough to transform the wall configuration from Bloch to the Néel. On the other hand, in other conditions when the DW has the Néel structure, the DW energy density is

$$\sigma_{\mathrm{DW}}(H_{\mathrm{IP}}) = \sigma_0 + 2\Delta K_{\mathrm{D}} - \pi\Delta M_{\mathrm{S}}|H_{\mathrm{IP}} + H_{\mathrm{DMI}}|. \tag{2}$$

In Eqs. (1) and (2), σ_0 is the Bloch DW energy, M_{S} is the saturation magnetization, K_{D} is the DW anisotropy energy density, and Δ is the DW width. Je *et al.* argued that if the domain wall motion occurs in the creep regime then the DW velocity is [15]

$$v = v_0 \exp\left(-\zeta H_{\mathrm{OP}}^{-\mu}\right), \tag{3}$$

where v_0 is the characteristic speed, μ is the creep scaling exponent which is 1/4 [44,50], and ζ is a scaling constant which exclusively is dependent on H_{IP} applied field via $\zeta = \zeta_0[\sigma(H_{\mathrm{IP}})/\sigma(0)]^{1/4}$. ζ_0 is a scaling constant.

In this way, when H_{IP} is equal and opposite to H_{DMI} the DW energy is maximum. Hence there will be a minimum in the velocity of the DW at that particular value of applied field, H_{offset}. On the basis of this simple model, $H_{\mathrm{offset}} = -H_{\mathrm{DMI}}$, and the velocity of DW will increase symmetrically around this offset field. Consequently, the radial symmetry of the DW creep is broken by H_{IP} and graphs of $v(H_{\mathrm{IP}})$ for DWs on opposite sides of the bubble will form mirrored offset pairs, as shown schematically in Fig. 5(a).

Results from asymmetric bubble expansion measurements on all the samples with different values of t_{Ir} are shown in Figs. 5(b)–5(h). Figure 5(i) shows the dependence of H_{offset}, measured as an average of the values obtained from the curves for the left- and right-moving DWs, on t_{Ir}. These data show the remarkable fact that H_{offset} drops significantly as soon as any Ir is introduced at the upper Co interface. Taking, for now, H_{offset} as an estimate for H_{DMI}, this indicates a weaker overall DMI. This is at variance with *ab initio* calculations [34] and some experimental studies [11] that lead us to expect that Pt and Ir will induce DMI of opposite sign, leading to an overall additive effect when placed on either side of a ferromagnetic layer [35]. Our result implies that the DMI induced by Ir is in fact more like that for Pt than that for Ta, which is expected

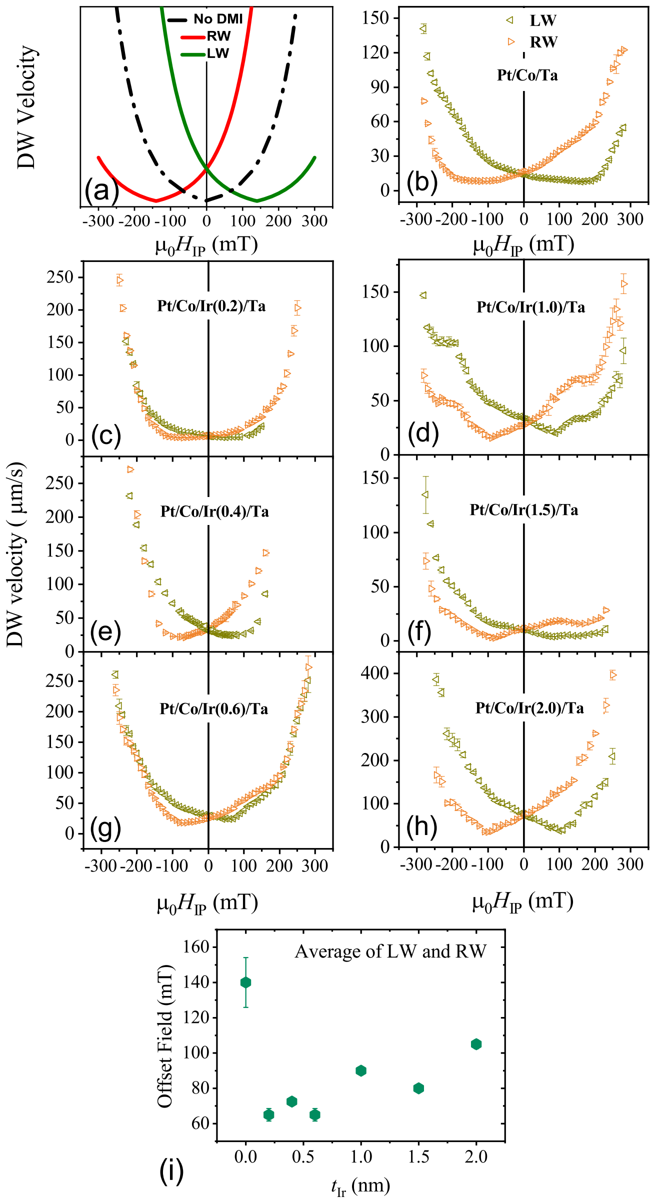

FIG. 5. Variation of DW velocity v with IP field H_{IP} for left- and right-moving DWs, LW, and RW, respectively. (a) Simulated from Eq. (3). When there is no DMI, v_{DW} has a minimum at zero in-plane field and rises symmetrically for opposite field directions. When DMI is present the minimum point is shifted to $\pm H_{\mathrm{offset}}$ depending on the direction of the DMI vector inside the wall. (b)–(h) Experimental data for left wall (green triangles) and right wall (orange triangles) for multilayers with different t_{Ir}. A lack of symmetry around the minimum points is obvious in most cases. (i) Average H_{offset} as a function of t_{Ir}.

to be small [8]. Germane to this, it is worth noting that two recent BLS studies also reported same sign of DMI for Co/Pt and Co/Ir interfaces [37,51].

Unlike the curves expected from Eqs. (1)–(3)—and other experimental results [16,21]—v does not show a symmetrical form on either side of H_{offset} in any case. Furthermore, for some films there are steplike anomalies. Another notable feature is that the curves for the left- and right-moving DWs meet up at high enough in-plane fields, which is also not expected on the basis of Fig. 5(a). Where none of these features can be explained with the theory of asymmetric bubble expansion in Ref. [15], some have also been seen in other experiments on different structures [25,26,30]. This suggests that the approach used in Eqs. (1) and (2) to define changes of DW energy with respect to H_{IP} is not universal and should be used with great care.

The in-plane field will eventually become strong enough to completely align the magnetization of the DW around the bubble in the direction of H_{IP}. According to the simple creep model embodied in Eqs. (1)–(3), beyond this point the two velocities for walls on either side of the bubble, v_{LW} and v_{RW}, will have a constant ratio, meaning that their difference, normalized to their sum, will saturate, as shown in Fig. 6(a). This behavior does not occur in our multilayers. Figures 6(b) and 6(c) show the variations of the velocity asymmetries for each sample with t_{Ir}. Every curve has a peak (instead of a plateau) after which the asymmetry declines. In some cases we were able to apply a strong enough H_{IP} to bring the asymmetry back to zero, at which value it saturates. The details of DW velocity variation are also subtly different for samples with thinner and thicker Ir layers: for larger t_{Ir} the peak is more cusplike. This return to symmetric expansion is also evident in Fig. 6(d), which shows a series of Kerr images for increasing in-plane field. The growth asymmetry (i.e., velocity asymmetry) initially increases, reaches a maximum value for $\mu_0 H_{\mathrm{IP}} \approx 100$ mT, and then decreases until the propagation of DWs is symmetrical again at $\mu_0 H_{\mathrm{IP}} \approx 250$ mT. This behavior is not limited to one sample or one nucleation point, so it cannot be related to any spatial variation of the magnetic parameters.

To complement the asymmetric bubble expansion measurements, we also used BLS to evaluate the strength of the DMI in each of our multilayers. An example of the BLS spectra is shown in Fig. 7(a), showing Stokes and anti-Stokes peaks. The nonreciprocal SW propagation in films with DMI leads to a frequency shift, Δf. This shift changes sign with magnetization direction. The black dashed-dotted line represents the expectation for the case when there is no DMI. Figure 7(b) shows Δf averaged over the two frequency shifts applying opposite saturating fields and measured for each different value of t_{Ir}. Δf decreases slightly as the Ir is inserted between Co and Ta layers, but again remains almost constant for thicker Ir layers when $t_{\mathrm{Ir}} > 0.5$ nm, reminiscent of Fig. 5(i). Such a large nonreciprocity of the SWs cannot be the result of surface anisotropy or dipolar effects. Surface anisotropy contributions come into play where $k_{\mathrm{SW}} t_{\mathrm{FM}} \ll 1$ (t_{FM} is ferromagnetic thickness) [52,53], and thus are negligible here due to the ultrathin Co layer. On the other hand, frequency shifts resulting from dipolar effects do not change sign with respect to the magnetization direction of the sample in question [54].

III. ASYMMETRIC BUBBLE EXPANSION THEORY

In this section, to go beyond the simple model expressed in Eqs. (1)–(3), we present a theoretical analysis of the dependence of the wall velocity as a function of in-plane applied

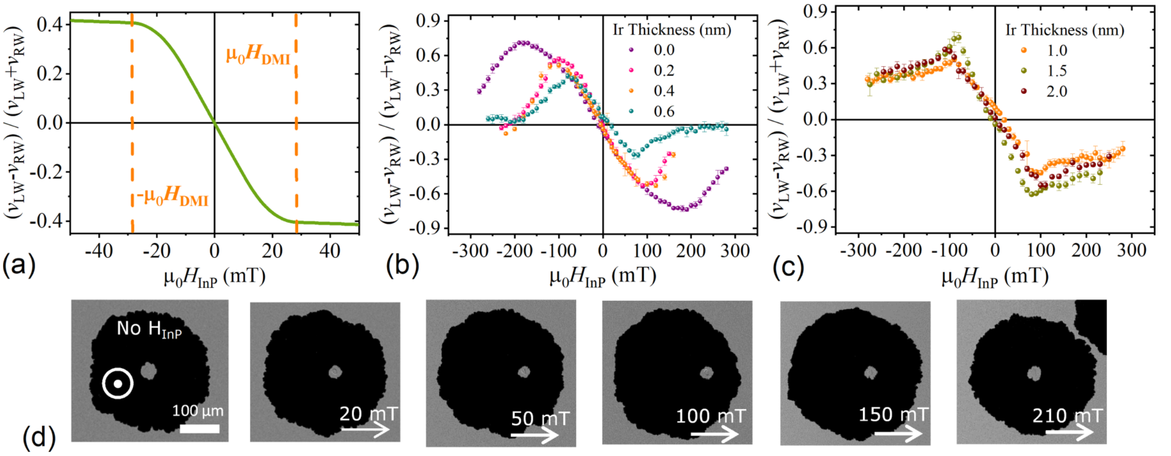

FIG. 6. Difference between right and left DW velocities normalized to their sum, $(v_{RW} - v_{LW})/(v_{RW} + v_{LW})$, as a function of IP field, (a) extracted from Eq. (3), which predicts a rise in the velocity asymmetry with H_{IP} that reaches saturation at high enough fields. Experimental results for multilayers with (b) thin and (c) thick Ir layers (plotted separately for clarity), which show no such saturation. (d) Kerr microscope images from Pt/Co/Ir(0.6)/Ta with increasing applied in-plane field. The propagated bubble domain changes from being symmetrical for zero IP field to asymmetrical growth for medium fields; then growth changes back to symmetrical for high enough magnetic fields. The domains are expanded with a OP field pulse of 6.5 mT. Pulse times are adjusted so that magnetic domains cover more or less the same area.

fields, as shown in Fig. 5. We consider the usual creep model,

$$v = v_0 \exp\left(-\frac{\Delta E}{k_B T}\right) \tag{4}$$

[cf. Eq. (3)], where the barrier energy has the universal form [46]

$$\Delta E = k_B T_d\left[\left(\frac{H_{OP}}{H_d}\right)^{-1/4} - 1\right]. \tag{5}$$

Here, $v_0 = v(H = H_d)$, H_d is the depinning field, and $k_B T_d$ is the characteristic pinning energy scale. H_{OP} is an OP field driving the DW motion or bubble expansion. Our analysis is based on the assumption that the dominant contribution to the in-plane field dependence comes from the variation in the depinning field, $H_d(H_{IP})$. We compute this quantity numerically using micromagnetics simulations [55,56] by following the method described in Ref. [57]. The simulation geometry comprises a 0.8-nm-thick ferromagnetic film with dimensions of 0.5 μm × 1 μm that is discretized using 512 × 1024 × 1 finite different cells. We used micromagnetic parameters consistent with the Pt/Co/Ta system, namely $M_s = 1.19$ MA/m and $A = 20$ pJ/m. The magnetic disorder is modeled using a grain structure where the perpendicular anisotropy constant, $K_u = K_{eff} + \frac{1}{2}\mu_0 M_s^2$, takes on a random value drawn from a uniform distribution centered about 1.38 MJ/m^3, with a 17.5% spread in the values. The average grain size is taken to be 10 nm, consistent at an order of magnitude level with our analysis of the TEM cross sections like those shown in Fig. 1, in which several nm scale grains can be seen. The disorder parameters are chosen to give depinning fields at $H_{IP} = 0$ that match experimental values as closely as possible. No stochastic thermal field was used.

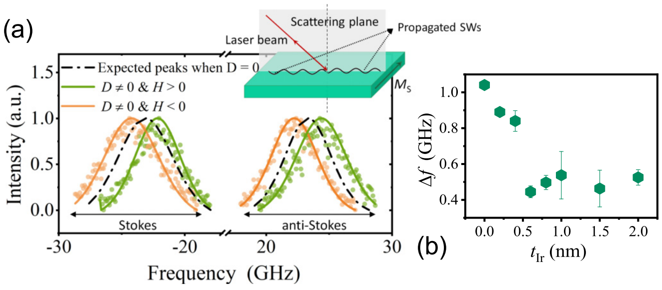

FIG. 7. Brillouin light scattering. (a) Normalized BLS spectra measured for Pt/Co/Ta at two equal and opposite applied fields of ∼1 T in orange and green. The black dashed line shows what is expected in case that there is no DMI in the sample. Symbols refer to experimental data and solid lines are Lorentzian fits. The panel at the top represents the Damon-Eshbach geometry which was used for measurements presented in this work. (b) Frequency shift Δf against Ir thickness t_{Ir}.

The depinning field is then estimated from the simulations as follows. For a given realization of the disorder, we relax an initially straight domain wall that runs along the width of the simulation grid in the y direction. The wall is positioned close to the center of the simulation grid ($x = 0$) and separates an up domain to the left ($x < 0$) and a down domain to the right ($x > 0$). To simulate an infinitely large system, periodic boundary conditions are applied along the y direction, while the magnetization is assumed to be uniform outside the simulation grid in the x direction. We include the dipolar fields from the magnetization outside the grid as an additional effective field. A uniform OP external field is applied and is increased from zero in increments of 2 mT, where the magnetization is relaxed using an energy minimization procedure at each increment. During this procedure, the wall gradually roughens and the up domain gradually expands toward the $x > 0$ direction. The depinning field is assigned to be the highest field reached before the wall depins and sweeps through the system in the x direction. This procedure is performed for 100 different realizations of the disorder for each value of the H_{IP} studied. The simulated variation in the depinning field, $H_d(H_{IP})$, for five different values of the DMI constant, D, is shown in Fig. 8. H_d has a maximum at a certain

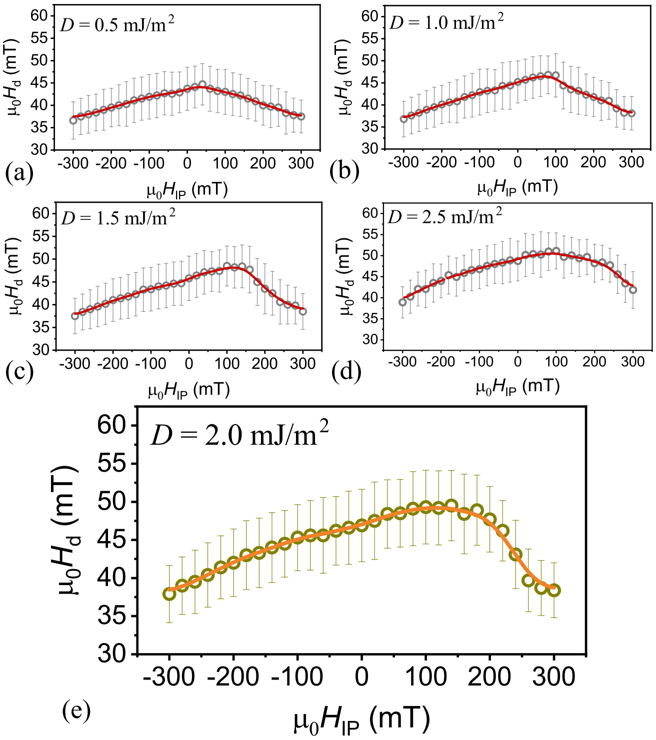

FIG. 8. Depinning field as a function of in-plane applied field from micromagnetics simulations for different values of the DMI constant, D: (a) 0.5 mJ/m^2, (b) 1.0 mJ/m^2, (c) 1.5 mJ/m^2, (d) 2.5 mJ/m^2, and (e) 2.0 mJ/m^2. The circles represent the average H_d value and the error bars indicate standard deviation. The solid (red) curve represents a smoothed function.

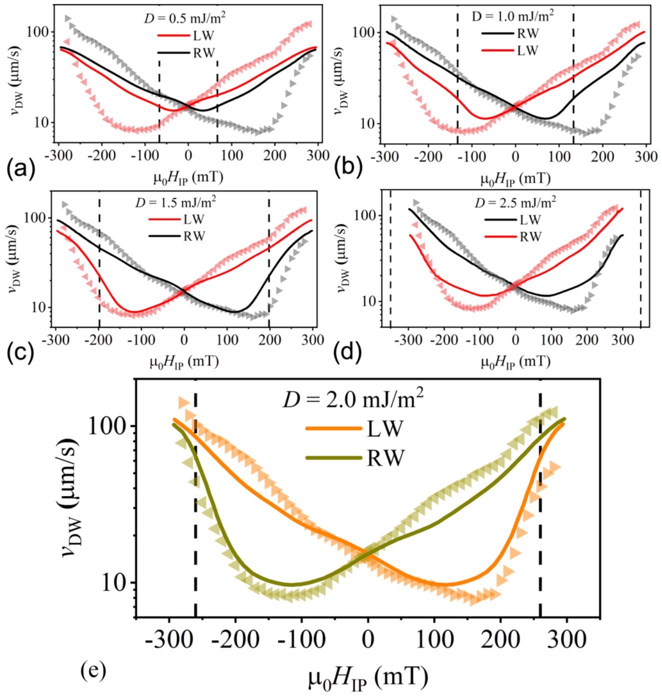

FIG. 9. Domain wall velocity, v, as a function of in-plane applied field, H_IP, for four different values of the DMI constant, D: (a) 0.5 mJ/m^2, (b) 1.0 mJ/m^2, (c) 1.5 mJ/m^2, (d) 2.5 mJ/m^2, and (e) 2.0 mJ/m^2. The triangles represent experimental data for the Pt/Co/Ta system (Fig. 5). The dashed vertical lines represent the DMI field extracted from simulation.

value of H_IP that increases as the DMI becomes stronger. This maximum value also has a close to linear dependence to D. The presence of the DMI leads to an asymmetric variation of H_d with respect to H_IP, where the asymmetry becomes more pronounced as D is increased. This variation can be tens of milliteslas over the field range studied, which can lead to significant variations in the energy barrier given in Eq. (5). We note that the functional form of $H_\mathrm{d}(H_\mathrm{IP})$ is reminiscent of the changes in the elastic energy of the domain wall [30].

A prediction of how the wall velocity varies with H_IP can be made by using Eqs. (4) and (5) along with $H_\mathrm{d}(H_\mathrm{IP})$ from Fig. 8. The results are presented in Fig. 9 for different values of D. The velocity curves are computed for each D value as follows. First, we perform a fit of Eq. (4) on the experimental $v(H_\mathrm{OP})$ data with the value of $H_\mathrm{d} = H_\mathrm{d,sim}$ obtained from simulation, which allows us to determine $v_0 = v_0^*$ and $T_\mathrm{d} = T_\mathrm{d}^*$. Second, we use these parameters $(H_\mathrm{d,sim}, v_0^*, T_\mathrm{d}^*)$ to calculate the value of $H_\mathrm{OP} = H_\mathrm{OP}^*$ in Eq. (5) such that the velocities match the experimental data at $H_\mathrm{IP} = 0$ in Fig. 5(b). The $v(H_\mathrm{IP})$ curves depicted in Fig. 9 were then obtained by using the smoothed function $H_\mathrm{d}(H_\mathrm{IP})$ (Fig. 8) in the expression for the energy barrier given in Eq. (5) in which we insert the values $T_\mathrm{d} = T_\mathrm{d}^*$ and $H = H_\mathrm{OP}^*$. The only freely adjustable parameter is D.

In the light of this, that the theoretical $v(H_\mathrm{IP})$ curve for $D = 2.0$ mJ/m^2 reproduces semiquantitatively the experimental data for the Pt/Co/Ta system [Fig. 9(f)] is remarkable. Besides capturing the overall shape of the asymmetry and the position of the velocity minimum, the curve also reproduces the fact that the velocities for the left and right wall converge toward one another as the magnitude of H_IP is increased. Such behavior is absent in previous models for the DMI-induced changes in the wall velocity [15], where the DMI enters simply as an effective magnetic field (which results only in a shift of the velocity curve along the H_IP axis). It is also important that the position of the velocity minimum does not coincide with the effective DMI field, $\mu_0 H_\mathrm{DMI} = D/M_\mathrm{s}\Delta$, the values for which are indicated in Fig. 9 by the vertical dashed lines (and computed from the micromagnetic parameters used in the simulations). This indicates that equating H_DMI with the field H_IP at which the velocity minimum occurs can lead to a significant underestimate of the DMI. These features are also present in the velocity curves for other values of D, as shown in Figs. 9(a)–9(d).

This modeling yields similar results to previous work based on considering elastic contributions to the DW energy [30]. Nevertheless, there is no established theory that gives a functional form $H_\mathrm{d}(\sigma_\mathrm{DW})$, where σ_DW is the DW energy density. In our approach we do not need to make any assumptions about how the depinning fields and domain wall (elastic) energies are related (although they most certainly are). Instead, we make use of the fact that the depinning field, a quantity that can be readily determined in experiment and simulation, enters explicitly into the universal form of the energy barrier given in Eq. (5). Calculating this depinning field is straightforward and its computed dependence on the in-plane field allows us to make predictions on how the wall

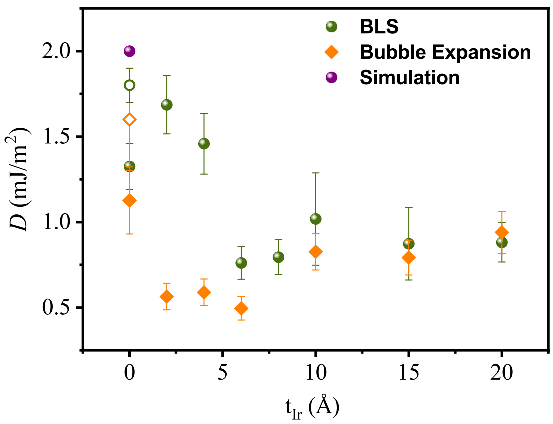

FIG. 10. Comparison of DMI results for the series of samples. Orange diamonds are the results obtained from taking the field of minimum asymmetric bubble expansion velocity as H_{DMI}. Green circles are the results from BLS. For $t_{\mathrm{Ir}} = 0$ the open shapes show the D value for BLS and bubble expansion when the measured M_{S} is substituted with the average value of other samples (i.e., excluding the dead layer effect). The purple circle shows the result of the simulation described in Sec. III.

velocity varies. Had we focused solely on the wall energy, we would have had to make additional assumptions on how this energy enters the energy barrier.

IV. DISCUSSION

Keeping all the above in mind, if we still assume that the $H_{\mathrm{IP}} = -H_{\mathrm{DMI}}$ for the velocity minimum, the DMI constant, D, can be calculated via $D = \mu_0 H_{\mathrm{DMI}} M_{\mathrm{S}} \Delta$ [3,16]. The frequency shift of the spin waves can also be used to get D as follows:

$$\Delta f = \left| \frac{g^{\parallel}\mu_B}{h} \right| \mathrm{sgn}(M_{\mathrm{OP}}) \frac{2D}{M_{\mathrm{S}}} k_{\mathrm{IP}}, \qquad (6)$$

where k_{IP} is the in-plane component of the wave vector of the light, $g^{\parallel}$ is the in-plane splitting factor, μ_{B} is the Bohr magneton, and h is the Planck constant [13]. The resulting DMI strengths assessed by the two methods are shown in Fig. 10.

In the past, results from BLS have shown stronger D than results from asymmetric bubble expansion on the same sample [24,58]. The same is true here for Ir thicknesses up to about 1 nm, although there is better agreement between the two methods for other values of t_{Ir}. This might be due to the different ways that BLS and asymmetric bubble expansion probe the film. Asymmetric bubble expansion studies growth of a bubble domain, the nucleation and propagation of which is sensitive to spatial variation of the film's properties on the scale of the DW width. Our simulation results also emphasize this sensitivity of DW creep to spatially fluctuating magnetic properties due to defects (i.e., disorder distributions). There can be seen a large standard deviation of calculated H_{d} values in Fig. 8 regardless of same input macroscopic experimental values. On the other hand, BLS measures difference in spin waves propagation in which local fluctuations of the properties are ineffective [59]. In this way, the resulting D can be considered to be an average value for the film, not just at the strongest pinning sites that control the creep motion. Simply put, DWs are localized objects, whereas spin waves are delocalized.

Taking a closer look at Fig. 10 reveals that there are still two similarities between the BLS and asymmetric bubble expansion results. First, both show a reduction of the net D value when comparing the samples having thick Ir—effectively a Pt/Co/Ir trilayer—with the zero Ir, i.e., Pt/Co/Ta trilayer. As briefly discussed above, this suggests that the DMI constant at an Ir/Co interface has the same sign as at a Pt/Co interface. The sign and strength changes of the DMI constant when one scans through 5d transition metals has been reported previously [8,60,61]. The DMI sign of a Pt/FM interface proved to be negative more often than not [21,29,34,62], which is equivalent to introducing left-handed chirality into the system. But the Ir/FM case is not as straightforward as Pt/FM interface. Initially, *ab initio* calculations proposed that Ir introduces the opposite chirality to Pt [33,34,63], which was supported by various experimental reports of additive effects [16,35,60,61,64]. Later on, the sign of DMI for Ir was debated when several experimental studies measured right-handed chirality in multilayers including Ir/Co [28,37,61].

The curious case of Ir does not end here, as other *ab initio* calculations showed that the chirality of Ir/FM interface differs when the adjacent ferromagnetic material changes from Fe (right-handed), to Co (left-handed), and Ni (right-handed) [65]. Ma *et al.* also measured opposite signs of D for Ir/Co and Ir/CoFeB interfaces [61]. Considering all these contradictory results about the sign of the DMI at Ir/FM interfaces, one wonders about the possible physical reasons for it. In this type of system, the DMI is considered to be mostly an interfacial effect. Partly, this interfacial sensitivity comes from dependence on the HM 5d states filling. For example, the DMI has opposite sign for W and Ta, with less-than-half-filled 5d states, in comparison with Pt and Au with more-than-half-filled 5d states [61]. In addition, the same 5d states hybridize with 3d orbitals in the adjacent ferromagnet and the changes in hybridization, as well as the alignment of Fermi levels across the FM/HM interface, will affect the DMI [33,65]. As DMI is sensitive to slight changes in any hybridization or Fermi alignment, controlling the interface quality on the atomic level might be needed to fix the DMI strength and even sign. In polycrystalline thin films, such as the ones in this paper, this much control over deposition is almost impossible as there is always unavoidable interdiffusion, or interface roughness which is changing from sample to sample and system to system. The situation is more crucial for Ir, since it is placed in the middle of elements having opposite DMI signs in 5d heavy metals, having seen electrons in its 5d orbitals.

Second, for $t_{\mathrm{Ir}} \gtrsim 0.5$ nm, not only are the measured D values from both methods in close agreement (within error bars and despite all mentioned anomalies), but also only weakly, if at all, dependent on t_{Ir}. This lack of dependence on t_{Ir} once it approaches this value was also observed for other material parameters such as those derived from field-induced DW motion fitted by universal creep and depinning regime functions [Figs. 3(c)–3(f)] or the coercive field [inset of Fig. 2(a)]. This seems reasonable in the light of the fact that the Ir layer is of extreme thinness when t_{Ir} is less than this value, and will not be completely continuous, such that the Co layer underneath remains in direct contact with Ta in some places. This will cause local variation in the value of interface dependent properties. Unfortunately, characterizing such very thin Ir layers by means of TEM cross sections is very challenging, and so we are not able to discuss the matter in a more quantitative way from an experimental point of view. Nevertheless, first-principles calculations suggest that 80% of the DMI strength is related to the first two monolayers of the HM layer [61]. Two monolayers of Ir in the (111) growth direction would be about 0.5 nm, the thickness after which the measured DMI constant does not change significantly. Changes of DMI with HM thickness and its saturation at high enough thicknesses was also reported for other multilayers [66,67]. A case closer to ours is one reported by Rowan-Robinson *et al.*, who observed this saturation for $t_{\mathrm{Ir}} > 0.4$ nm for Pt/Co/Ir(0.0–2.5 nm)/Pt multilayers[68], which is in good agreement with our measurements here.

It is good to keep in mind that, for the case of $t_{\mathrm{Ir}} = 0$, Co is in direct contact with Ta and reportedly this interface forms a magnetic deadlayer [38–41,69–75], which eventually leads to an underestimation of M_{S} due to the reduction of the effective thickness of the ferromagnetic material. This is reflected in the calculation of other parameters for this stack including the DMI strength, D. Nevertheless, if we take the average value of saturation magnetization as this sample's M_{S}, the DMI strength will be $D_{\mathrm{BLS}} = 1.8 \pm 0.1$ mJ/m^2 and $D_{\mathrm{ABE}} = 1.6 \pm 0.3$ mJ/m^2 for BLS and asymmetric bubble expansion (naïvely taking H_{DMI} to be the velocity minimum), respectively. The D_{BLS} value is very close to $D_{\mathrm{sim}} = 2.0$ mJ/m^2, the value used in the simulations in Fig. 9(f).

V. CONCLUSION

The experimental data presented here gives a full picture of the DW dynamics and DMI of polycrystalline Pt/Co/Ir(t_{Ir})/Ta multilayers. The chirality of the DWs proved to be left handed using asymmetric bubble expansion, which is the usual behavior reported for DWs in both theoretical [33,34,76] and experimental [6,14,60] studies of Co/Pt interfaces, also for Pt/Co/Ir multilayers [16,29,58]. The experimental $v(H_{\mathrm{IP}})$ curves for these films that were acquired using asymmetrical bubble expansion [Figs. 5(b)–5(h)] do not have the form expected from the simple creep model [15] that is often used to analyze such data [Fig. 5(a)]. In that model, the dependence of v on H_{IP} appears exclusively in the DW energy. Meanwhile, Soucaille *et al.* [24] reported variation of DW roughness with H_{IP}, and Pellegren *et al.* considered the role of DW elastic energy [30]. Based on our observation of universal scaling (Fig. 4), we introduced asymmetric variation of the depinning field, H_{d}, with H_{IP}. This model reproduces both lack of symmetry of the $v(H_{\mathrm{IP}})$ curve about their minima and the closing up of these curves for left- and right-moving DWs at high IP field. In the case of $t_{\mathrm{Ir}} = 0$, where we have made a direct quantitative comparison, this approach to analyzing the asymmetric bubble expansion data gives much better agreement with BLS results on the same sample than the naïve process of measuring the field at which a velocity minimum occurs.

Data association with this paper are available for download at Ref. [77].

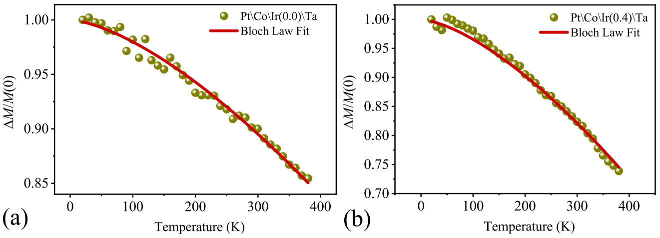

FIG. 11. Temperature dependence of magnetization in (a) Pt/Co/Ta and (b) Pt/Co/Ir(0.4)/Ta multilayers. The red line shows the Bloch law fit in each case.

ACKNOWLEDGMENTS

We thank Simone Moretti and Rebeca Díaz-Pardo for their help. This work was supported by European Community under the Seventh Framework Programme–The People Programme, Multi-ITN "Wall" (Grant No. 608031), and partially supported by the DARPA Topological Excitations in Electronics (TEE) program (No. R18-687-0004).

APPENDIX A: EXCHANGE STIFFNESS MEASUREMENT

We measured the temperature dependence of the saturation magnetization $M_{\mathrm{s}}(T)$ in order to determine the exchange stiffness A. This may be fitted to a Bloch law $M_{\mathrm{s}}(T) = M_0(1 - bT^{3/2})$, in which M_0 is the saturation magnetization at zero kelvin, in order to extract the coefficient b. The exchange stiffness is then given by [78]

$$A = \frac{nk_{\mathrm{B}}S^2}{a}\left(\frac{C}{b}\right)^{2/3}, \tag{A1}$$

where $n = 4$ is the coordination number for an fcc lattice, S is the spin per atom, C is a constant that takes the value 0.0294 for an fcc lattice, and a is the lattice constant. The data and fit for Ir thicknesses of $t_{\mathrm{Ir}} = 0$ and 0.4 nm are shown in Fig. 11. These fits yielded values for the two samples that average to $A = 17 \pm 2$ pJ/m.

APPENDIX B: CONFIRMING CREEP MOTION

In this appendix, we show additional data on DW creep motion. We checked that the samples were in the creep regime both in the absence and presence of (high) IP field in order to ensure that our asymmetric bubble expansion

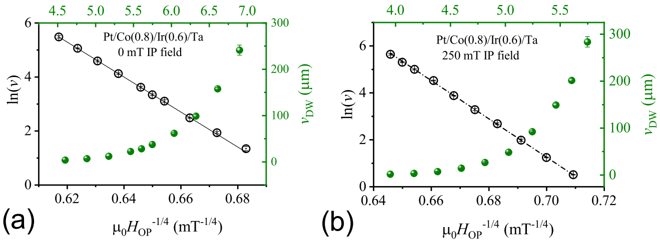

FIG. 12. Investigation of creep propagation of the DWs in a bubble domain for $t_{\mathrm{Ir}} = 0.6$ nm. (a) Without any applied in-plane field and (b) in the presence of a high in-plane field: $\mu_0 H_x = 250$ mT. In both cases the creep scaling law is well-obeyed.

measurements were not affected by the changing IP field. A linear variation of $\ln v$ as a function of $H^{-1/4}$ verifies DW creep propagation [44], as shown in Fig. 3(b) for zero in-plane field. We also performed measurements with an in-plane field of $\mu_0 H_x = 250$ mT, as shown here in Fig. 12 for the sample with $t_{\text{Ir}} = 0.6$ nm. In both the zero-field and $\mu_0 H_x = 250$ mT field case, this scaling is well obeyed by the sample.

[1] S. S. P. Parkin and S.-H. Yang, Memory on the racetrack, Nat. Nanotechnol. **10**, 195 (2015).

[2] A. Fert, V. Cros, and J. Sampaio, Skyrmions on the track, Nat. Nanotechnol. **8**, 152 (2013).

[3] A. Thiaville, S. Rohart, É. Jué, V. Cros, and A. Fert, Dynamics of Dzyaloshinskii domain walls in ultrathin magnetic films, EPL (Europhys. Lett.) **100**, 57002 (2012).

[4] A. V. Khvalkovskiy, V. Cros, D. Apalkov, V. Nikitin, M. Krounbi, K. A. Zvezdin, A. Anane, J. Grollier, and A. Fert, Matching domain-wall configuration and spin-orbit torques for efficient domain-wall motion, Phys. Rev. B **87**, 020402 (2013).

[5] K.-S. Ryu, L. Thomas, S.-H. Yang, and S. S. P. Parkin, Chiral spin torque at magnetic domain walls, Nat. Nanotechnol. **8**, 527 (2013).

[6] S. Emori, U. Bauer, S.-M. Ahn, E. Martinez, and G. S. D. Beach, Current-driven dynamics of chiral ferromagnetic domain walls, Nat. Mater. **12**, 611 (2013).

[7] E. Martinez, S. Emori, and G. S. D. Beach, Current-driven domain wall motion along high perpendicular anisotropy multilayers: The role of the Rashba field, the spin Hall effect, and the Dzyaloshinskii-Moriya interaction, Appl. Phys. Lett. **103**, 072406 (2013).

[8] J. Torrejon, J. Kim, J. Sinha, S. Mitani, M. Hayashi, M. Yamanouchi, and H. Ohno, Interface control of the magnetic chirality in CoFeB/MgO heterostructures with heavy-metal underlayers, Nat. Commun. **5**, 4655 (2014).

[9] K. Garello, I. M. Miron, C. O. Avci, F. Freimuth, Y. Mokrousov, S. Blügel, S. Auffret, O. Boulle, G. Gaudin, and P. Gambardella, Symmetry and magnitude of spin–orbit torques in ferromagnetic heterostructures, Nat. Nanotechnol. **8**, 587 (2013).

[10] S. Meckler, N. Mikuszeit, A. Preßler, E. Y. Vedmedenko, O. Pietzsch, and R. Wiesendanger, Real-Space Observation of a Right-Rotating Inhomogeneous Cycloidal Spin Spiral by Spin-Polarized Scanning Tunneling Microscopy in a Triple Axes Vector Magnet, Phys. Rev. Lett. **103**, 157201 (2009).

[11] G. Chen, T. Ma, A. T. N'Diaye, H. Kwon, C. Won, Y. Wu, and A. K. Schmid, Tailoring the chirality of magnetic domain walls by interface engineering, Nat. Commun. **4**, 2671 (2013).

[12] O. Boulle, J. Vogel, H. Yang, S. Pizzini, D. de Souza Chaves, A. Locatelli, T. O. Menteş, A. Sala, L. D. Buda-Prejbeanu, O. Klein, M. Belmeguenai, Y. Roussigné, A. Stashkevich, S. M. Chérif, L. Aballe, M. Foerster, M. Chshiev, S. Auffret, I. M. Miron, and G. Gaudin, Room-temperature chiral magnetic skyrmions in ultrathin magnetic nanostructures, Nat. Nanotechnol. **11**, 449 (2016).

[13] H. T. Nembach, J. M. Shaw, M. Weiler, E. Jué, and T. J. Silva, Linear relation between Heisenberg exchange and interfacial Dzyaloshinskii-Moriya interaction in metal films, Nat. Phys. **11**, 825 (2015).

[14] M. Belmeguenai, J.-P. Adam, Y. Roussigné, S. Eimer, T. Devolder, J. V. Kim, S. M. Cherif, A. Stashkevich, and A. Thiaville, Interfacial Dzyaloshinskii-Moriya interaction in perpendicularly magnetized Pt/Co/AlO$_x$ ultrathin films measured by Brillouin light spectroscopy, Phys. Rev. B **91**, 180405 (2015).

[15] S.-G. Je, D.-H. Kim, S.-C. Yoo, B.-C. Min, K.-J. Lee, and S.-B. Choe, Asymmetric magnetic domain-wall motion by the Dzyaloshinskii-Moriya interaction, Phys. Rev. B **88**, 214401 (2013).

[16] A. Hrabec, N. A. Porter, A. J. Wells, M.-J. Benitez, G. Burnell, S. McVitie, D. McGrouther, T. A. Moore, and C. H. Marrows, Measuring and tailoring the Dzyaloshinskii-Moriya interaction in perpendicularly magnetized thin films, Phys. Rev. B **90**, 020402 (2014).

[17] T. J. Gallagher, K. Ju, and F. B. Humphrey, State identification and stability of magnetic bubbles with unit winding number, J. Appl. Phys. **50**, 997 (1979).

[18] F. H. de Leeuw, R. van den Doel, and U. Enz, Dynamic properties of magnetic domain walls and magnetic bubbles, Rep. Prog. Phys. **43**, 689 (1980).

[19] Y. P. Kabanov, Y. L. Iunin, V. I. Nikitenko, A. J. Shapiro, R. D. Shull, L. Y. Zhu, and C. L. Chien, In-plane field effects on the dynamics of domain walls in ultrathin Co films with perpendicular anisotropy, IEEE Trans. Magn. **46**, 2220 (2010).

[20] D. Petit, P. R. Seem, M. Tillette, R. Mansell, and R. P. Cowburn, Two-dimensional control of field-driven magnetic bubble movement using Dzyaloshinskii-Moriya interactions, Appl. Phys. Lett. **106**, 022402 (2015).

[21] R. A. Khan, P. M. Shepley, A. Hrabec, A. W. J. Wells, B. Ocker, C. H. Marrows, and T. A. Moore, Effect of annealing on the interfacial Dzyaloshinskii-Moriya interaction in Ta/CoFeB/MgO trilayers, Appl. Phys. Lett. **109**, 132404 (2016).

[22] T. H. Pham, J. Vogel, J. Sampaio, M. Vaňatka, J.-C. Rojas-Sánchez, M. Bonfim, D. S. Chaves, F. Choueikani, P. Ohresser, E. Otero, A. Thiaville, and S. Pizzini, Very large domain wall velocities in Pt/Co/GdOx and Pt/Co/Gd trilayers with Dzyaloshinskii-Moriya interaction, EPL (Europhys. Lett.) **113**, 67001 (2016).

[23] D.-Y. Kim, D.-H. Kim, J. Moon, and S.-B. Choe, Determination of magnetic domain-wall types using Dzyaloshinskii-Moriya-interaction-induced domain patterns, Appl. Phys. Lett. **106**, 262403 (2015).

[24] R. Soucaille, M. Belmeguenai, J. Torrejon, J.-V. Kim, T. Devolder, Y. Roussigné, S.-M. Chérif, A. A. Stashkevich, M. Hayashi, and J.-P. Adam, Probing the Dzyaloshinskii-Moriya interaction in CoFeB ultrathin films using domain wall creep and Brillouin light spectroscopy, Phys. Rev. B **94**, 104431 (2016).

[25] R. Lavrijsen, D. M. F. Hartmann, A. van den Brink, Y. Yin, B. Barcones, R. A. Duine, M. A. Verheijen, H. J. M. Swagten, and B. Koopmans, Asymmetric magnetic bubble expansion under in-plane field in Pt/Co/Pt: Effect of interface engineering, Phys. Rev. B **91**, 104414 (2015).

[26] M. Vaňatka, J.-C. Rojas-Sánchez, J. Vogel, M. Bonfim, M. Belmeguenai, Y. Roussigné, A. Stashkevich, A. Thiaville, and

S. Pizzini, Velocity asymmetry of Dzyaloshinskii domain walls in the creep and flow regimes, J. Phys.: Condens. Matter **27**, 326002 (2015).

[27] D. Lau, V. Sundar, J.-G. Zhu, and V. Sokalski, Energetic molding of chiral magnetic bubbles, Phys. Rev. B **94**, 060401 (2016).

[28] F. Ajejas, V. Křižáková, D. de Souza Chaves, J. Vogel, P. Perna, R. Guerrero, A. Gudin, J. Camarero, and S. Pizzini, Tuning domain wall velocity with Dzyaloshinskii-Moriya interaction, Appl. Phys. Lett. **111**, 202402 (2017).

[29] P. M. Shepley, H. Tunnicliffe, K. Shahbazi, G. Burnell, and T. A. Moore, Magnetic properties, domain-wall creep motion, and the Dzyaloshinskii-Moriya interaction in Pt/Co/Ir thin films, Phys. Rev. B **97**, 134417 (2018).

[30] J. P. Pellegren, D. Lau, and V. Sokalski, Dispersive Stiffness of Dzyaloshinskii Domain Walls, Phys. Rev. Lett. **119**, 027203 (2017).

[31] S. Woo, M. Mann, A. J. Tan, L. Caretta, and G. S. D. Beach, Enhanced spin-orbit torques in Pt/Co/Ta heterostructures, Appl. Phys. Lett. **105**, 212404 (2014).

[32] S. Woo, K. Litzius, B. Krüger, M.-Y. Im, L. Caretta, K. Richter, M. Mann, A. Krone, R. M. Reeve, M. Weigand, P. Agrawal, I. Lemesh, M.-A. Mawass, P. Fischer, M. Kläui, and G. S. D. Beach, Observation of room-temperature magnetic skyrmions and their current-driven dynamics in ultrathin metallic ferromagnets, Nat. Mater. **15**, 501 (2016).

[33] V. Kashid, T. Schena, B. Zimmermann, Y. Mokrousov, S. Blügel, V. Shah, and H. G. Salunke, Dzyaloshinskii-Moriya interaction and chiral magnetism in $3d-5d$ zigzag chains: Tight-binding model and *ab initio* calculations, Phys. Rev. B **90**, 054412 (2014).

[34] H. Yang, A. Thiaville, S. Rohart, A. Fert, and M. Chshiev, Anatomy of Dzyaloshinskii-Moriya Interaction at Co/Pt Interfaces, Phys. Rev. Lett. **115**, 267210 (2015).

[35] C. Moreau-Luchaire, C. Moutafis, N. Reyren, J. Sampaio, C. A. F. Vaz, N. Van Horne, K. Bouzehouane, K. Garcia, C. Deranlot, P. Warnicke, P. Wohlhüter, J.-M. George, M. Weigand, J. Raabe, V. Cros, and A. Fert, Additive interfacial chiral interaction in multilayers for stabilization of small individual skyrmions at room temperature, Nat. Nanotechnol. **11**, 444 (2016).

[36] A. Soumyanarayanan, M. Raju, A. L. Gonzalez Oyarce, A. K. C. Tan, M.-Y. Im, A. P. Petrović, P. Ho, K. H. Khoo, M. Tran, C. K. Gan, F. Ernult, and C. Panagopoulos, Tunable room-temperature magnetic skyrmions in Ir/Fe/Co/Pt multilayers, Nat. Mater. **16**, 898 (2017).

[37] N.-H. Kim, J. Jung, J. Cho, D.-S. Han, Y. Yin, J.-S. Kim, H. J. M. Swagten, and C.-Y. You, Interfacial Dzyaloshinskii-Moriya interaction, surface anisotropy energy, and spin pumping at spin orbit coupled Ir/Co interface, Appl. Phys. Lett. **108**, 142406 (2016).

[38] C.-W. Cheng, W. Feng, G. Chern, C. M. Lee, and T.-H. Wu, Effect of cap layer thickness on the perpendicular magnetic anisotropy in top MgO/CoFeB/Ta structures, J. Appl. Phys. **110**, 033916 (2011).

[39] J. Sinha, M. Hayashi, A. J. Kellock, S. Fukami, M. Yamanouchi, H. Sato, S. Ikeda, S. Mitani, S.-H. Yang, S. S. P. Parkin, and H. Ohno, Enhanced interface perpendicular magnetic anisotropy in Ta/CoFeB/MgO using nitrogen doped Ta underlayers, Appl. Phys. Lett. **102**, 242405 (2013).

[40] S. Y. Jang, C.-Y. You, S. H. Lim, and S. R. Lee, Annealing effects on the magnetic dead layer and saturation magnetization in unit structures relevant to a synthetic ferrimagnetic free structure, J. Appl. Phys. **109**, 013901 (2011).

[41] S. Bandiera, R. C. Sousa, B. Rodmacq, and B. Dieny, Asymmetric interfacial perpendicular magnetic anisotropy in Pt/Co/Pt trilayers, IEEE Magn. Lett. **2**, 3000504 (2011).

[42] C. Ederer, M. Komelj, M. Fähnle, and G. Schütz, Theory of induced magnetic moments and x-ray magnetic circular dichroism in Co-Pt multilayers, Phys. Rev. B **66**, 094413 (2002).

[43] P. J. Metaxas, J. P. Jamet, A. Mougin, M. Cormier, J. Ferré, V. Baltz, B. Rodmacq, B. Dieny, and R. L. Stamps, Creep and Flow Regimes of Magnetic Domain-Wall Motion in Ultrathin Pt/Co/Pt Films with Perpendicular Anisotropy, Phys. Rev. Lett. **99**, 217208 (2007).

[44] S. Lemerle, J. Ferré, C. Chappert, V. Mathet, T. Giamarchi, and P. Le Doussal, Domain Wall Creep in an Ising Ultrathin Magnetic Film, Phys. Rev. Lett. **80**, 849 (1998).

[45] P. Chauve, T. Giamarchi, and P. Le Doussal, Creep and depinning in disordered media, Phys. Rev. B **62**, 6241 (2000).

[46] V. Jeudy, A. Mougin, S. Bustingorry, W. Savero Torres, J. Gorchon, A. B. Kolton, A. Lemaître, and J.-P. Jamet, Universal Pinning Energy Barrier for Driven Domain Walls in Thin Ferromagnetic Films, Phys. Rev. Lett. **117**, 057201 (2016).

[47] V. Jeudy, R. Díaz Pardo, W. Savero Torres, S. Bustingorry, and A. B. Kolton, Pinning of domain walls in thin ferromagnetic films, Phys. Rev. B **98**, 054406 (2018).

[48] R. Diaz Pardo, W. Savero Torres, A. B. Kolton, S. Bustingorry, and V. Jeudy, Universal depinning transition of domain walls in ultrathin ferromagnets, Phys. Rev. B **95**, 184434 (2017).

[49] A. Kirilyuk, J. Ferré, V. Grolier, J. P. Jamet, and D. Renard, Magnetization reversal in ultrathin ferromagnetic films with perpendicular anisotropy, J. Magn. Magn. Mater. **171**, 45 (1997).

[50] K.-J. Kim, J.-C. Lee, S.-M. Ahn, K.-S. Lee, C.-W. Lee, Y. J. Cho, S. Seo, K.-H. Shin, S.-B. Choe, and H.-W. Lee, Interdimensional universality of dynamic interfaces, Nature (London) **458**, 740 (2009).

[51] D. Lau, J. P. Pellegren, H. Nembach, J. Shaw, and V. Sokalski, Disentangling factors governing Dzyaloshinskii domain wall creep in Co/Ni thin films using $\mathrm{Pt}_x\mathrm{Ir}_{1-x}$ seedlayers, Phys. Rev. B **98**, 184410 (2018).

[52] A. A. Stashkevich, M. Belmeguenai, Y. Roussigné, S. M. Cherif, M. Kostylev, M. Gabor, D. Lacour, C. Tiusan, and M. Hehn, Experimental study of spin-wave dispersion in Py/Pt film structures in the presence of an interface Dzyaloshinskii-Moriya interaction, Phys. Rev. B **91**, 214409 (2015).

[53] O. Gladii, M. Haidar, Y. Henry, M. Kostylev, and M. Bailleul, Frequency nonreciprocity of surface spin wave in permalloy thin films, Phys. Rev. B **93**, 054430 (2016).

[54] J.-H. Moon, S.-M. Seo, K.-J. Lee, K.-W. Kim, J. Ryu, H.-W. Lee, R. D. McMichael, and M. D. Stiles, Spin-wave propagation in the presence of interfacial Dzyaloshinskii-Moriya interaction, Phys. Rev. B **88**, 184404 (2013).

[55] J. Leliaert, B. Van de Wiele, A. Vansteenkiste, L. Laurson, G. Durin, L. Dupré, and B. Van Waeyenberge, Current-driven domain wall mobility in polycrystalline permalloy nanowires: A numerical study, J. Appl. Phys. **115**, 233903 (2014).

[56] A. Vansteenkiste, J. Leliaert, M. Dvornik, M. Helsen, F. Garcia-Sanchez, and B. Van Waeyenberge, The design and verification of MuMax3, AIP Adv. **4**, 107133 (2014).

[57] J.-V. Kim and M.-W. Yoo, Current-driven skyrmion dynamics in disordered films, Appl. Phys. Lett. **110**, 132404 (2017).

[58] K. Zeissler, M. Mruczkiewicz, S. Finizio, J. Raabe, P. M. Shepley, A. V. Sadovnikov, S. A. Nikitov, K. Fallon, S. McFadzean, S. McVitie, T. A. Moore, G. Burnell, and C. H. Marrows, Pinning and hysteresis in the field dependent diameter evolution of skyrmions in Pt/Co/Ir superlattice stacks, Sci. Rep. **7**, 15125 (2017).

[59] I. Gross, L. J. Martínez, J.-P. Tetienne, T. Hingant, J.-F. Roch, K. Garcia, R. Soucaille, J. P. Adam, J.-V. Kim, S. Rohart, A. Thiaville, J. Torrejon, M. Hayashi, and V. Jacques, Direct measurement of interfacial Dzyaloshinskii-Moriya interaction in $x|$CoFeB$|$MgO heterostructures with a scanning NV magnetometer ($x =$ Ta, TaN, and W), Phys. Rev. B **94**, 064413 (2016).

[60] K.-S. Ryu, S.-H. Yang, L. Thomas, and S. S. P. Parkin, Chiral spin torque arising from proximity-induced magnetization, Nat. Commun. **5**, 3910 (2014).

[61] X. Ma, G. Yu, C. Tang, X. Li, C. He, J. Shi, K. L. Wang, and X. Li, Interfacial Dzyaloshinskii-Moriya Interaction: Effect of 5*d* Band Filling and Correlation with Spin Mixing Conductance, Phys. Rev. Lett. **120**, 157204 (2018).

[62] A. W. J. Wells, P. M. Shepley, C. H. Marrows, and T. A. Moore, Effect of interfacial intermixing on the Dzyaloshinskii-Moriya interaction in Pt/Co/Pt, Phys. Rev. B **95**, 054428 (2017).

[63] K. Yamamoto, A.-M. Pradipto, K. Nawa, T. Akiyama, T. Ito, T. Ono, and K. Nakamura, Interfacial Dzyaloshinskii-Moriya interaction and orbital magnetic moments of metallic multilayer films, AIP Adv. **7**, 056302 (2017).

[64] M. Baćani, M. A. Marioni, J. Schwenk, and H. J. Hug, How to measure the local Dzyaloshinskii Moriya interaction in skyrmion thin film multilayers, arXiv:1609.01615.

[65] A. Belabbes, G. Bihlmayer, F. Bechstedt, S. Blügel, and A. Manchon, Hund's Rule-Driven Dzyaloshinskii-Moriya Interaction at 3*d*–5*d* Interfaces, Phys. Rev. Lett. **117**, 247202 (2016).

[66] X. Ma, G. Yu, X. Li, T. Wang, D. Wu, K. S. Olsson, Z. Chu, K. An, J. Q. Xiao, K. L. Wang, and X. Li, Interfacial control of Dzyaloshinskii-Moriya interaction in heavy metal/ferromagnetic metal thin film heterostructures, Phys. Rev. B **94**, 180408 (2016).

[67] S. Tacchi, R. E. Troncoso, M. Ahlberg, G. Gubbiotti, M. Madami, J. Åkerman, and P. Landeros, Interfacial Dzyaloshinskii-Moriya Interaction in Pt/CoFeB Films: Effect of the Heavy-Metal Thickness, Phys. Rev. Lett. **118**, 147201 (2017).

[68] R. M. Rowan-Robinson, A. A. Stashkevich, Y. Roussigné, M. Belmeguenai, S.-M. Chérif, A. Thiaville, T. P. A. Hase, A. T. Hindmarch, and D. Atkinson, The interfacial nature of proximity-induced magnetism and the Dzyaloshinskii-Moriya interaction at the Pt/Co interface, Sci. Rep. **7**, 16835 (2017).

[69] J. Yu, X. Qiu, Y. Wu, J. Yoon, P. Deorani, J. M. Besbas, A. Manchon, and H. Yang, Spin orbit torques and Dzyaloshinskii-Moriya interaction in dual-interfaced Co-Ni multilayers, Sci. Rep. **6**, 32629 (2016).

[70] B. Zhang, A. Cao, J. Qiao, M. Tang, K. Cao, X. Zhao, S. Eimer, Z. Si, N. Lei, Z. Wang, X. Lin, Z. Zhang, M. Wu, and W. Zhao, Influence of heavy metal materials on magnetic properties of Pt/Co/heavy metal tri-layered structures, Appl. Phys. Lett. **110**, 012405 (2017).

[71] H. Sato, M. Yamanouchi, S. Ikeda, S. Fukami, F. Matsukura, and H. Ohno, Perpendicular-anisotropy CoFeB-MgO magnetic tunnel junctions with a MgO/CoFeB/Ta/CoFeB/MgO recording structure, Appl. Phys. Lett. **101**, 022414 (2012).

[72] S. Y. Jang, S. H. Lim, and S. R. Lee, Magnetic dead layer in amorphous CoFeB layers with various top and bottom structures, J. Appl. Phys. **107**, 09C707 (2010).

[73] K. Oguz, P. Jivrajka, M. Venkatesan, G. Feng, and J. M. D. Coey, Magnetic dead layers in sputtered $\mathrm{Co_{40}Fe_{40}B_{20}}$ films, J. Appl. Phys. **103**, 07B526 (2008).

[74] Y.-H. Wang, W.-C. Chen, S.-Y. Yang, K.-H. Shen, C. Park, M.-J. Kao, and M.-J. Tsai, Interfacial and annealing effects on magnetic properties of CoFeB thin films, J. Appl. Phys. **99**, 08M307 (2006).

[75] S. Ingvarsson, G. Xiao, S. S. P. Parkin, and W. J. Gallagher, Thickness-dependent magnetic properties of $\mathrm{Ni_{81}Fe_{19}}$, $\mathrm{Co_{90}Fe_{10}}$, and $\mathrm{Ni_{65}Fe_{15}Co_{20}}$ thin films, J. Magn. Magn. Mater. **251**, 202 (2002).

[76] F. Freimuth, S. Blügel, and Y. Mokrousov, Berry phase theory of Dzyaloshinskii-Moriya interaction and spin-orbit torques, J. Phys.: Condens. Matter **26**, 104202 (2014).

[77] https://doi.org/10.5518/539.

[78] S. Chikazumi, *Physics of Ferromagnetism*, 2nd ed. (Oxford University Press, Oxford, 1997).